Response of a fluid-immersed microcantilever close to a deformable sample

R.J. Clarke[1], V. Bachtiar[2], T-C. Lee[1], J.E. Cater[1], and J. Minton[3]

[1] *Department of Engineering Science, University of Auckland, New Zealand*

[2] *Department of Mechanical Engineering, University of Melbourne, Australia and*

[3] *Department of Applied Mathematics and Theoretical Physics, University of Cambridge, UK*

(Dated: October 20, 2014)

Abstract

The importance of hydrodynamics upon the response of a microcantilever immersed in a viscous fluid has been well established [1, 8]. It has previously been shown that the presence of a nearby solid surface can significantly alter a microcantilever's non-contact response, through microcantilever–surface hydrodynamic interactions [9–12]. In cases where the nearby surface is deformable, rather than rigid, we expect to see further changes in the microcantilever's response. Hence we here use the Boundary Element Method to numerically compute the elastohydrodynamics of a microcantilever oscillating close to a compliant body, over a range of different operating conditions. We then determine the effect of the elastohydrodynamics upon the cantilever's thermal spectrum, using Fluctuation-Dissipation Theorem. Our findings demonstrate that the flow regime, as determined by the properties of the microcantilever, can substantially dictate the extent to which the compliance of a given sample is evident in the thermal spectra. We expect these findings to be of interest in areas such as atomic force microscopy, microsensing and microrheology.

PACS numbers:

Keywords: Microcantilever, Scanning Probe Microscopy, Elastohydrodynamics, Fluctuation-Dissipation Theorem

I. INTRODUCTION

The ability to predict the frequency response of oscillating microcantilevers is important to a number of different microdevice technologies, including scanning probe microscopy and radio frequency switches. The importance of hydrodynamics upon the frequency response of an oscillating microcantilever has been well established. In a landmark theoretical paper, Sader [1] developed a model to describe the thermal response of a microcantilever immersed in a viscous fluid, and later demonstrated its ability to faithfully reproduce spectra obtained experimentally [3]. Subsequent theoretical studies demonstrated how the presence of rigid surfaces [2, 9, 11–14], or neighbouring microcantilevers [4–7] (where such arrays of microcantilevers have applications in biosensing), can modify the hydrodynamics, and consequently the microcantilever's frequency response.

The situation where the nearby surface is deformable has been less well studied. This is potentially important, not only because many atomic force microscope measurements are conducted on soft biological specimens, but also due to some recent efforts to develop non-contact micromechanical measurement techniques using oscillating microcantilevers [15]. In the scenario where the sample is a thin elastic layer, and is located sufficiently close to an oscillating microcantilever (as is the case in [15]), the hydrodynamics can be approximated using oscillatory squeeze film theory. For general time dependent driving of the microcantilever under such circumstances, it has been shown that an integro-differential equation can be derived to describe the elastohydrodynamics [16]. However, such squeeze film models are somewhat limited in their applicability to microcantilevers with high natural frequencies. This is due to the fact that the magnitude of hydrodynamic forces generated by flows outside of the squeeze film region increase with oscillation frequency, and so can become comparable with the squeeze film hydrodynamic forces within the gap (which are required to dominate for the squeeze film approximation to hold).

Therefore in this study we generalise the theoretical treatment of the elastohydrodynamics to consider elastohydrodynamics outside of the squeeze film regime. Moreover, we allow the sample to undergo general linearly-elastic deformations. This is achieved by coupling together boundary-integral representations of Oscillatory Stokes Flow for the hydrodynamics, and the Navier Equations for the elastic deformations of the sample. These are solved numerically using the Boundary Element Method, which allows us to examine the impact

of the microcantilever properties upon the elastohydrodynamics. We can then examine the extent to which compliant effects are evident in the microcantilever's thermal response, through the use of the Fluctuation-Dissipation Theorem [4, 5, 12].

II. THEORY

We work in a Cartesian coordinate system (x_1^*, x_2^*, x_3^*). (Note that asterisks denote dimensional quantities throughout.) We consider a microcantilever with characteristic cross-sectional width R^*, length L^*, and which is aligned with the x_3^*-axis. This is immersed in a Newtonian fluid that has dynamic viscosity μ^* and density ρ^*. The microcantilever fluctuates with amplitude C^*, frequency ω^*, has a surface denoted by $\mathcal{S}^{(1)}$ and lies a minimum distance H^* from an elastic sample with surface denoted $\mathcal{S}^{(2)}$. This elastic sample has density ρ_s^*, Poisson Ratio ν, Young's Modulus E^*, and undergoes elastic displacements of characteristic size $A^* \ll R^*, H^*$. We assume that the resonant frequency of the microcantilever is high, $\omega_0^* \gg 1$, and that the sample is much more compliant than the microcantilever. In what follows we non-dimensionalise independent variables in the following way:

$$x_1^* = R^* x_1, \quad x_2^* = R^* x_2, \quad x_3^* = L^* x_3, \quad t^* = t/\omega_0^*, \quad \omega^* = \omega_0^* \omega. \tag{1}$$

It also proves useful to define a dimensionless microcantilever-sample distance, $\Delta \equiv H^*/R^*$ and density ratio $\Delta\rho^* = \rho_s^*/\rho^*$. In keeping with earlier studies [1, 9, 11, 12], we consider the dynamics in a cross-sectional plane, and assume that the geometry of neither the microcantilever or the sample vary too rapidly in the longitudinal (i.e. x_3-) direction, compared with changes in the cross-sectional plane. This allows us to consider the dynamics as largely two-dimensional (although the methodology discussed below can readily be extended to consider more fully three-dimensional scenarios).

A. Microcantilever Dynamics

We assume that the microcantilever is constrained to fluctuate in the x_2-direction only, where its driven deflections are oscillatory $\mathrm{Re}\,(w^*(x_3)\exp(i\omega t))$. We non-dimensionalise deflection, w^*, according to $w^* = C^* w$ and, following [1], model the deflections of the cantilever using

Euler–Bernoulli beam theory

$$\frac{d^4w}{dx_3^4} - B^4 w = 0, \quad B(\omega) = c_1\sqrt{\omega}\,(1 + T\Gamma(\gamma_f))^{1/4} \tag{2}$$

($c_1 \approx 1.875$), with $T = R^{*\,2}\rho^*/m_c^*$, where m_c^* is the mass per unit length of the microcantilever, and $\gamma_f = \bar{R}_f^{1/2}\omega^{1/2}$ is a non-dimensional measure of the flow inertia at a given frequency. $\bar{R}_f = \omega_0^*\,\rho^* R^{*\,2}/\mu^*$ we refer to as the characteristic flow inertia. Also, $\Gamma(\gamma_f) = D(\gamma_f)/i\gamma_f^2$ is the hydrodynamic function, where

$$D = \int_{\mathcal{S}^{(1)}} \boldsymbol{f}\cdot\hat{\boldsymbol{x}}_2\, dl(\boldsymbol{x})$$

is the hydrodynamic drag, with $\boldsymbol{f} = \boldsymbol{\sigma}_f\cdot\boldsymbol{n}$ the hydrodynamic traction ($\boldsymbol{\sigma}_f$ is the non-dimensional flow stress tensor; see §II B, and $\boldsymbol{n}$ a unit normal to the microcantilever surface). We determine the Brownian-induced oscillations of the microcantilever using the Fluctuation-Dissipation Theorem [4, 12]. This states that the Thermal Spectrum, $P(\omega)$, for the slope of the cantilever at its tip ($x_3 = 1$) is related to deterministic response of the cantilever under application of a point torque at this location. This response is known as the Susceptivity, χ. Specifically, the Fluctuation-Dissipation Theorem states that

$$P(\omega) = \sqrt{2|\mathrm{Im}(\chi)|/\omega} \tag{3}$$

where Im denotes that imaginary parts are to be taken, and $\chi = dw(1)/dx_3$ under the boundary conditions

$$w(0) = \frac{dw}{dx_3}(0) = \frac{d^4w}{dx_3^4}(1) = 0, \quad \frac{d^3w}{dx_3^3}(1) = 1, \tag{4}$$

i.e. clamped conditions at $x_3 = 0$, together with stress-free and point-torque conditions at $x_3 = 1$. Hence

$$\chi(\omega) = \frac{\cos B(\omega)\sinh B(\omega) + \sin B(\omega)\cosh B(\omega)}{B(\omega)(1 + \cos B(\omega)\cosh B(\omega))}. \tag{5}$$

B. Flow Dynamics

The motion of the microcantilever generates oscillatory flows $\mathrm{Re}\,(\boldsymbol{v}^*(\boldsymbol{x})\exp(\mathrm{i}\omega t))$ where $\boldsymbol{v}^*(\boldsymbol{x}) = (v_1^*(\boldsymbol{x}), v_2^*(\boldsymbol{x}))$. When we non-dimensionalise flow velocity, pressure, and stress tensor $\boldsymbol{\sigma}_f^* = -p^*\boldsymbol{I} + \boldsymbol{\nabla}\boldsymbol{v}^* + (\boldsymbol{\nabla}\boldsymbol{v}^*)^T$ in the following manner

$$\boldsymbol{v}^* = (A^*\omega^*)\boldsymbol{v}, \quad p^* = (\mu^*\omega^*A^*/R^*)p, \quad \boldsymbol{\sigma}_f^* = (\mu^*\omega^*A^*/R^*)\boldsymbol{\sigma}_f^*,$$

then the incompressible flow satisfies the (non-dimensional) unsteady Stokes Flow equations [1, 11]

$$\lambda_f^2 \boldsymbol{v} = -\boldsymbol{\nabla} p + \nabla^2 \boldsymbol{v}, \quad \boldsymbol{\nabla} \cdot \boldsymbol{v} = 0, \tag{6}$$

$\lambda_f = \sqrt{i}\gamma_f$, where γ_f is as defined beneath (2). This quantity can be seen to measure the importance of unsteady flow inertia, as compared with viscous effects. The flow is subject to no-slip and impermeability flow conditions on the surfaces of the microcantilever $\mathcal{S}^{(1)}$ and elastic sample $\mathcal{S}^{(2)}$, i.e.

$$\boldsymbol{v}(\boldsymbol{x}) = \begin{cases} \hat{\boldsymbol{x}}_2, & \boldsymbol{x} \in \mathcal{S}^{(1)}, \\ d\boldsymbol{u}'/dt, & \boldsymbol{x} \in \mathcal{S}^{(2)}, \end{cases} \tag{7}$$

where $\boldsymbol{u}'$ is the sample's elastic displacement. These flow equations can be recast into boundary integral form [17]

$$v_j(\boldsymbol{x}_0) = -\frac{1}{2\pi} \int_{\mathcal{S}} f_i(\boldsymbol{x}) S_{ij}(\hat{\boldsymbol{x}}; \lambda) \mathrm{d}l(\boldsymbol{x}) + \frac{1}{2\pi} \int_{\mathcal{S}} v_i(\boldsymbol{x}) T_{ijk}(\hat{\boldsymbol{x}}; \lambda) n_k \mathrm{d}l(\boldsymbol{x}), \quad \boldsymbol{x}_0 \in \mathcal{S} \tag{8}$$

where $\mathcal{S} = \mathcal{S}^{(1)} \cup \mathcal{S}^{(2)}$, $\hat{\boldsymbol{x}} = \boldsymbol{x} - \boldsymbol{x}_0 = (\hat{x}_1, \hat{x}_2)$ and $\boldsymbol{n} = (n_1, n_2)$ is the unit outward normal to the surface of integration. The exact form of the Green's Tensors S_{ij} are given by [18], from which T_{ijk} can be computed (Appendix A).

C. Sample Deformations

The hydrodynamic forces produced by the flow generate oscillatory small-strain elastic displacements in the sample, $\mathrm{Re}\left(\boldsymbol{u}^*(\boldsymbol{x}) \exp(\mathrm{i}\omega t)\right)$ where $\boldsymbol{u}^*(\boldsymbol{x}) = (u_1^*(\boldsymbol{x}), u_2^*(\boldsymbol{x}))$. If we non-dimensionalise the elastic displacement and stress, $\boldsymbol{\sigma}_s^*$, in the following way

$$\boldsymbol{u}^* = A^* \boldsymbol{u}, \quad \boldsymbol{\sigma}_s^* = (E^* A^*/R^*) \boldsymbol{\sigma}_s,$$

the non-dimensional elastic displacement is governed by the unsteady Navier's Equations

$$\lambda_s^2 \boldsymbol{u} = \frac{1}{1-2\nu} \boldsymbol{\nabla} \left(\boldsymbol{\nabla} \cdot \boldsymbol{u}\right) + \nabla^2 \boldsymbol{u}, \tag{9}$$

with $\lambda_s = \mathrm{i}\gamma_s$. Here $\gamma_s = \omega \bar{R}_s$ is a non-dimensional measure of the unsteady inertia in the elastic body, where $\bar{R}_s = \omega_0^* R^* \sqrt{2\rho_s^*(1+\nu)/E^*}$ we will refer to as the characteristic elastic inertia. This is subject to continuity of traction at the surface of the elastic body

$$\Lambda \boldsymbol{g}(\boldsymbol{x}) = \boldsymbol{f}(\boldsymbol{x}), \quad \boldsymbol{x} \in \mathcal{S}^{(2)}, \tag{10}$$

where $\Lambda = \omega^{-1}\Lambda_0$, with $\Lambda_0 = E^*/\mu^*\omega_0^*$ referred to here as the characteristic effective stiffness. and $\boldsymbol{g} \equiv \boldsymbol{\sigma}_s \cdot \boldsymbol{n}$ with $\boldsymbol{n}$ a unit normal to the surface $\mathcal{S}^{(2)}$.

The elasticity equations can be recast into the following boundary-integral form

$$2(1-\nu)u_j(\boldsymbol{x}_0) = -\frac{1}{2\pi}\int_{\mathcal{S}^{(2)}} g_i(\boldsymbol{x})K_{ij}(\hat{\boldsymbol{x}};\lambda)\mathrm{d}l(\boldsymbol{x}) + \frac{1}{2\pi}\int_{\mathcal{S}^{(2)}} u_i(\boldsymbol{x})Q_{ijk}(\hat{\boldsymbol{x}};\lambda)n_k\mathrm{d}l(\boldsymbol{x}), \quad (11)$$

($j = 1, 2$ and using Einstein notation for summation), where $\boldsymbol{x}_0 \in \mathcal{S}^{(2)}$. The Green's Tensors T_{ijk} and Q_{ijk} for the elasticity equations, i.e. Kelvin Solutions, are given by [19].

D. Elastohydrodynamics

Under the boundary conditions specified by (7) and (10), we arrive at the following pair of coupled boundary-integral equations describing the elastohydrodynamics of the system

$$\begin{aligned} v_j(\boldsymbol{x}_0) = &-\frac{1}{2\pi}\int_{\mathcal{S}^{(1)}} f_i(\boldsymbol{x})S_{ij}(\hat{\boldsymbol{x}};\lambda)\mathrm{d}l(\boldsymbol{x}) + \frac{1}{2\pi}\int_{\mathcal{S}^{(1)}} T_{2jk}(\hat{\boldsymbol{x}};\lambda)n_k\mathrm{d}l(\boldsymbol{x}) \\ &- \frac{1}{2\pi}\int_{\mathcal{S}^{(2)}} f_i(\boldsymbol{x})S_{ij}(\hat{\boldsymbol{x}};\lambda)\mathrm{d}l(\boldsymbol{x}) + \frac{\mathrm{i}}{2\pi}\int_{\mathcal{S}^{(2)}} u_i(\boldsymbol{x})T_{ijk}(\hat{\boldsymbol{x}};\lambda)n_k\mathrm{d}l(\boldsymbol{x}), \quad (12a) \end{aligned}$$

for $\boldsymbol{x}_0 \in \mathcal{S}$, alongside

$$2(1-\nu)u_j(\boldsymbol{x}_0) = -\frac{\Lambda^{-1}}{2\pi}\int_{\mathcal{S}^{(2)}} f_i(\boldsymbol{x})K_{ij}(\hat{\boldsymbol{x}};\lambda)\mathrm{d}l(\boldsymbol{x}) + \frac{1}{2\pi}\int_{\mathcal{S}^{(2)}} u_i(\boldsymbol{x})Q_{ijk}(\hat{\boldsymbol{x}};\lambda)n_k\mathrm{d}l(\boldsymbol{x}), \quad (12b)$$

when $\boldsymbol{x}_0 \in \mathcal{S}^{(2)}$.

III. NUMERICAL METHOD

In order to numerically solve the coupled integral equations given in (12), we discretise the surface of the microcantilever and sample into N_1 and N_2 discrete straight boundary elements, $\mathcal{S}^{(1)} = \left(\mathcal{S}_1^{(1)}, \ldots, \mathcal{S}_{N_1}^{(1)}\right)$ and $\mathcal{S}^{(2)} = \left(\mathcal{S}_1^{(2)}, \ldots, \mathcal{S}_{N_2}^{(2)}\right)$. Assuming that traction and displacement are constant over each element, we can define the following vectors of unknowns

$$\boldsymbol{f}^{(1)} = (\boldsymbol{f}(\boldsymbol{x}_1^{(1)}), \ldots, \boldsymbol{f}(\boldsymbol{x}_{N_1}^{(1)}))^T,\ \boldsymbol{f}^{(2)} = (\boldsymbol{f}(\boldsymbol{x}_1^{(2)}), \ldots, \boldsymbol{f}(\boldsymbol{x}_{N_2}^{(2)}))^T,\ \boldsymbol{U} = (\boldsymbol{u}(\boldsymbol{x}_1^{(2)}), \ldots, \boldsymbol{u}(\boldsymbol{x}_{N_2}^{(2)}))^T \quad (13)$$

(superscript T denotes a transpose), where $\boldsymbol{f} = (f_1, f_2)$, $\boldsymbol{u} = (u_1, u_2)$. The collocation points on the kth element of surfaces $\mathcal{S}^{(1)}$ and $\mathcal{S}^{(2)}$ are denoted $\boldsymbol{x}_k^{(1)}$, $\boldsymbol{x}_k^{(2)}$, respectively, and

are taken to be the mid-points of that element. By setting $\boldsymbol{x}_0$ to take values $\boldsymbol{x}_k^{(1)}$ and $\boldsymbol{x}_k^{(2)}$ in the boundary-integral representations of the flow and elastic deformation (12), we consequently obtain the following linear system

$$\begin{pmatrix} \left(\boldsymbol{I}_1 - \boldsymbol{T}^{(11)}\right)\boldsymbol{V} \\ -\boldsymbol{T}^{(21)}\boldsymbol{V} \\ \boldsymbol{0} \end{pmatrix} = \begin{pmatrix} \boldsymbol{S}^{(11)} & \boldsymbol{S}^{(12)} & \mathrm{i}\boldsymbol{T}^{(12)} \\ \boldsymbol{S}^{(21)} & \boldsymbol{S}^{(22)} & (\mathrm{i}\boldsymbol{T}^{(22)} - \boldsymbol{I}_2) \\ \boldsymbol{0} & \Lambda^{-1}\boldsymbol{K}^{(22)} & (\boldsymbol{Q}^{(22)} - c\boldsymbol{I}_2) \end{pmatrix} \begin{pmatrix} \boldsymbol{f}^{(1)} \\ \boldsymbol{f}^{(2)} \\ \boldsymbol{U} \end{pmatrix}, \tag{14}$$

where $c = 2(1-\nu)$, $\boldsymbol{V} = (0, 1, \ldots 0, 1)$ is the $(1 \times N_1)$-sized vector of prescribed velocity on the microcantilever surface, $\boldsymbol{I}_1$ and $\boldsymbol{I}_2$ are the $N_1 \times N_1$ and $N_2 \times N_2$ identity matrices, respectively. The sub-matrices are defined by

$$\boldsymbol{G}^{(\alpha\beta)}(2(k-1)+p, 2(m-1)+q) = -\frac{1}{2\pi}\int_{S_m^{(\beta)}} G_{pq}(\boldsymbol{x}, \boldsymbol{x}_k^{(\alpha)})\mathrm{d}l(\boldsymbol{x}), \tag{15}$$

with $\alpha, \beta, p, q = 1$ or 2, $k = 1 \ldots 2N_\alpha, m = 1 \ldots 2N_\beta$.

Computations were performed using $N_1 = N_2 = 1024$, with numerical convergence verified using $N_1 = N_2 = 2048$. Construction of the BEM matrices was parallelised, with the total computational time across all five cases amounting to about 600 CPU hours.

IV. RESULTS AND DISCUSSION

Recall that the important non-dimensional quantities that parameterise the elastohydrodynamics are given by:

$$\Lambda_0 = E^*/\mu^*\omega_0^*,\ \bar{R}_f = \rho^*\omega_0^*(R^*)^2/\mu^*,\ \bar{R}_s = \omega_0^* R^*\sqrt{2\rho_s^*(1+\nu)/E^*},\ T = (R^*)^2\rho^*/m_c^*,\ \Delta = H^*/R^*. \tag{16}$$

In Table I we illustrate how, for a sample with the same material properties (i.e. E^*, ρ_s^* and ν), these non-dimensional parameters can take very different values depending upon the properties of the microcantilever. For definiteness, we consider a sample with an initially circular cross-sectional shape, and radius 10μm (although there is nothing special about this particular choice, and in Appendix A 2 we demonstrate similar trends in the thermal spectra for an elliptically-shaped sample). In what follows we show that the values of the above non-dimensional parameters (16) are central to the emergence of compliant effects in the thermal spectra.

Case	E^* (kg/ms^2)	R^* (m)	ω_0^* (1/s)	H^* (m)	$\bar{R}_f$	T	Λ_0	$\bar{R}_s$	Δ
A1	10^4	10^{-5}	10^5	$2\times10^{-6}, 10^{-5}$	10	1	100	0.51	0.2, 1
A2	10^4	$10^{-5.5}$	10^6	$2\times10^{-6.5}, 10^{-5.5}$	10	1	10	1.61	0.2, 1
A3	10^4	10^{-5}	10^6	$2\times10^{-6}, 10^{-5}$	100	1	10	5.1	0.2, 1
B1	10^3	$10^{-5.5}$	10^6	$2\times10^{-6.5}, 10^{-5.5}$	10	1	1	5.1	0.2, 1
B2	10^3	$10^{-5.5}$	10^5	$10^{-6.5}$, $2\times10^{-6.5}, 10^{-5.5}$	1	1	10	0.51	0.1, 0.2, 1
B3	10^3	10^{-5}	10^5	$2\times10^{-6}, 10^{-5}$	10	1	10	1.61	0.2, 1

TABLE I: Example parameter values for a microcantilever, natural frequency ω_0^* and characteristic width R^*, oscillating close to a material with Young's modulus E^*. In all cases the immersing fluid has the properties of water, i.e. density $\rho^* = 10^3$ kg/m^3 and dynamic viscosity $\mu^* = 10^{-3}$ kg/ms, and the sample has density $\rho_s^* = 10^3$ kg/m^3 and Poisson ratio $\nu = 0.3$.

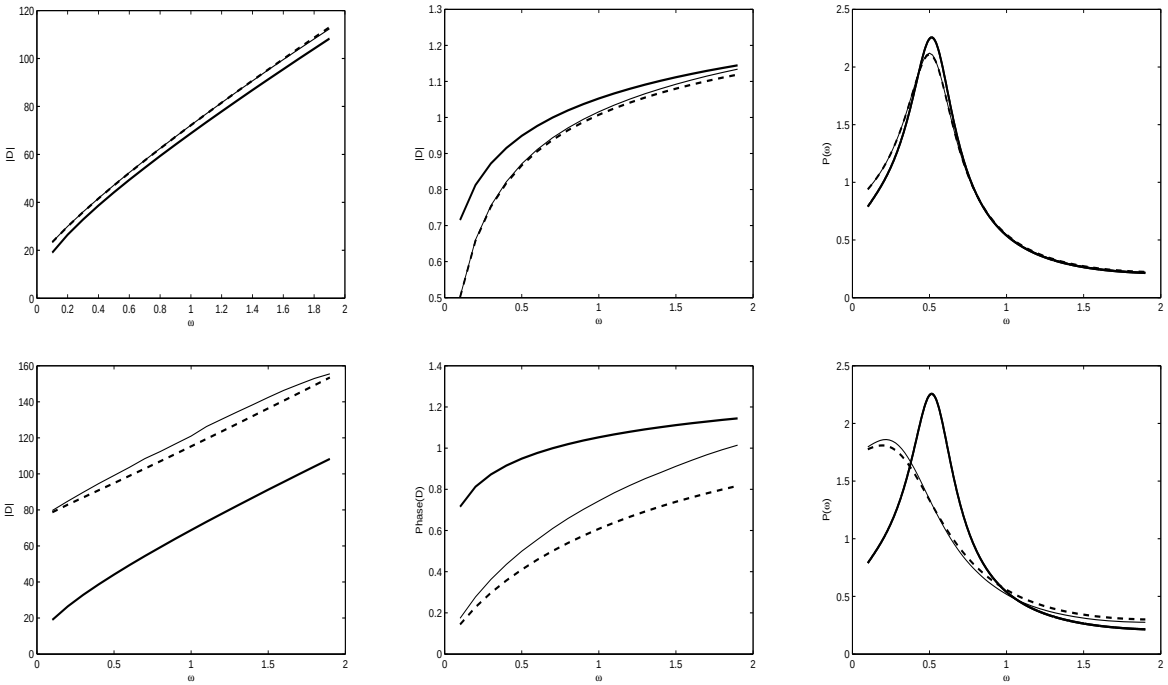

FIG. 1: Case A1: Modulus of Drag (left column) and Phase of Drag (middle column) exerted upon the microcantilever, as well as corresponding thermal spectra (right column), predicted when $\Lambda_0 = 100$, $\bar{R}_f = 10$, $\bar{R}_s = 0.51$, where (first row) $\Delta = 1$, (second row) $\Delta = 0.2$.

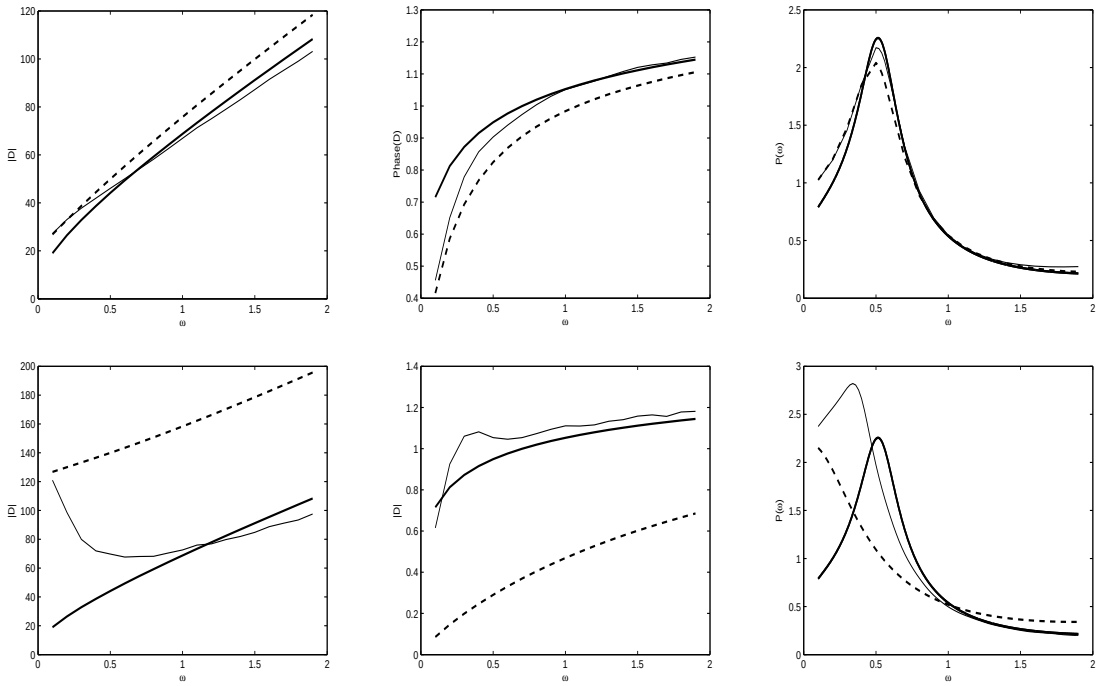

FIG. 2: Case A2: Modulus of Drag (left column) and Phase of Drag (middle column) exerted upon the microcantilever, as well as corresponding thermal spectra (right column), predicted when $\Lambda_0 = 10$, $\bar{R}_f = 10$, $\bar{R}_s = 1.61$, where (first row) $\Delta = 1$, (second row) $\Delta = 0.2$. Vertical dashed-dotted lines on the drag plots indicate the frequency of the resonant peak in the thermal spectrum.

In Figures 1–5 we plot the magnitude and phase of the hydrodynamic loading on the microcantilever as a function of oscillation frequency (thin, solid line). For reference we also plot the loading on the microcantilever in the absence of the sample (thick, solid line), and in the case where the sample is rigid (thick, dashed line). Alongside these hydrodynamic profiles, we also present the associated thermal spectra, as computed using Fluctuation–Dissipation Theory (3). We do so for two samples, A and B, which have Elastic Moduli $E^* = 10^4 \text{kg/ms}^2$ (10kPa) and $E^* = 10^3$ kg/ms^2 (1kPa), respectively. For each sample, we consider several different scenarios, corresponding to microcantilevers with differing properties. These are labelled as Cases A1–A3, and Cases B1–B3 (see Table I). Moreover, for each case we examine moderate microcantilever–sample separation $\Delta = 1$, and small separation, $\Delta = 0.2$ (for Case B2, we also examine the larger separation $\Delta = 2$).

Case A1 is presented in Figure 1, and corresponds to microcantilever properties ($R^* = 10\mu$m, $\omega_0^* = 10^5$/s) that result in moderate characteristic unsteady inertia in the flow ($\bar{R}_f = 10$),

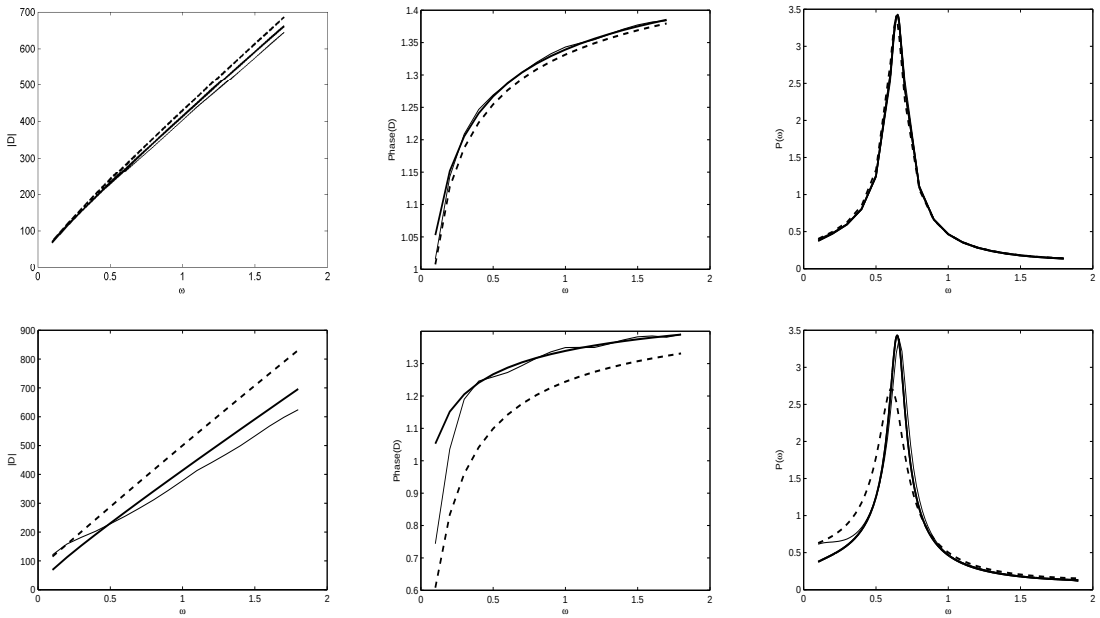

FIG. 3: Case A3: Modulus of Drag (Left Column) and Phase of Drag (Middle Column) exerted upon the microcantilever, as well as corresponding thermal spectra (Right Column), predicted when $\Lambda_0 = 10$, $\bar{R}_f = 100$, $\bar{R}_s = 5.1$ and (first row) $\Delta = 1$, (second row) $\Delta = 0.2$.

relatively high characteristic effective stiffness ($\Lambda_0 = 100$), and only a small degree of characteristic unsteady inertia in the elastic solid ($\bar{R}_s = 0.51$). At moderate microcantilever–sample separations ($\Delta = 1$, top row), we see that the hydrodynamic loadings largely follow the inelastic profile (thick dashed line). This trend is reflected in the corresponding thermal spectrum, which is almost indistinguishable from that predicted in the presence of an inelastic sample. When we decrease the separation distance to $\Delta = 0.2$ (Figure 1, bottom row), we observe some deviation in the hydrodynamic profiles away from the inelastic limit, although the impact upon the thermal spectrum is minimal.

For the same Sample A, if we now consider a slightly narrower, and stiffer microcantilever ($R^* \sim 3\mu$m, $\omega_0^* = 10^6$), as described by Case A2, we begin to observe noticeable compliant effects. The unsteady inertia in the flow is the same as in Case A1 ($\bar{R}_f = 10$), however, the effective stiffness has decreased ($\Lambda_0 = 10$), and the elastic inertia has increased to $\bar{R}_s = 1.61$. Figure 2 demonstrates the impact of these changes upon both the hydrodynamic loading and, consequently, the thermal spectra. At the larger of the two separations ($\Delta = 1$, top row), we observe that the hydrodynamic loading transitions between the inelastic limit

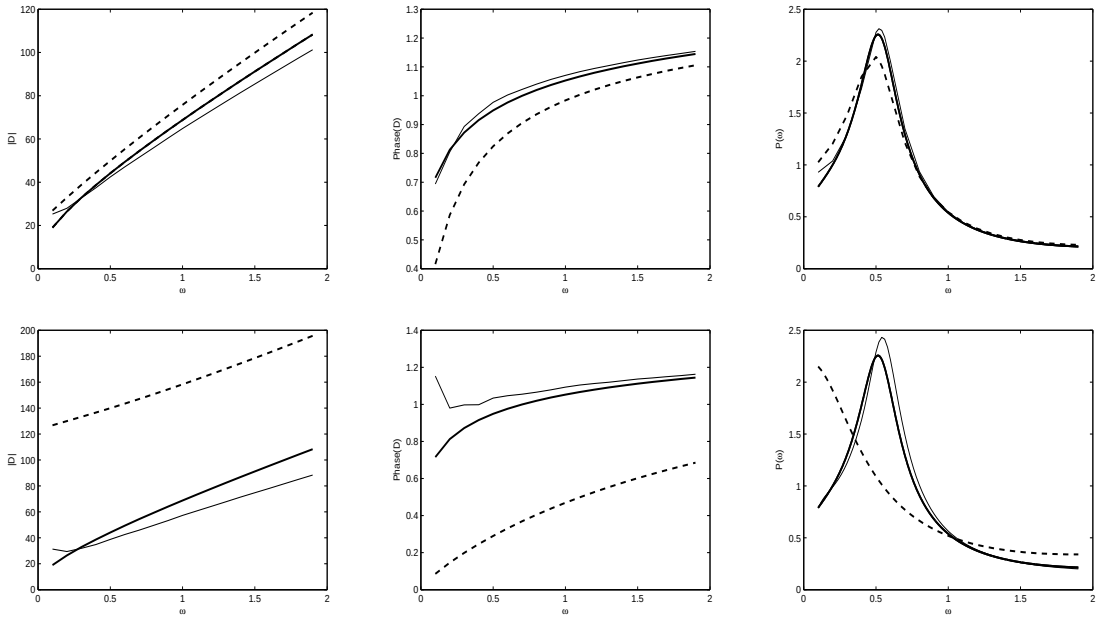

FIG. 4: Case B1: Modulus of Drag (Left Column) and Phase of Drag (Middle Column) exerted upon the microcantilever, as well as corresponding thermal spectra (Right Column), predicted when $\Lambda_0 = 1$, $\bar{R}_f = 10$, $\bar{R}_s = 5.1$ and (first row) $\Delta = 1$, (second row) $\Delta = 0.2$.

(thick dashed line) at lower frequencies and the sample-free limit (thick solid line) at higher frequencies. Comparable behaviour is observed in the thermal spectrum, the peak of which is located between the inelastic and sample-free spectra. However, at these separations the two limiting cases remain relatively close together, and so it is debatable whether these differences in spectra would be noticeable in the presence of typical levels of experimental noise. When we move the microcantilever closer to the sample ($\Delta = 0.2$, bottom row), however, the inelastic and sample-free limits become more distinct, and the influence of compliance upon the hydrodynamic loading becomes far more noticeable. The compliant hydrodynamic profiles are now well-removed from the inelastic limit, and tend towards the sample-free limit at higher frequencies. Compliant effects are now clearly distinguisable in the microcantilever's thermal response, which is now different from both the inelastic, and sample-free, spectra. The presence of the surface is observed to reduce the resonant frequency as compared with the sample-free spectra, although to a lesser degree for the compliant surface, an effect previously reported in experiments [15].

In Case A3 we keep the microcantilever's resonant frequency at $\omega_0^* = 10^6/\text{s}$, but increase

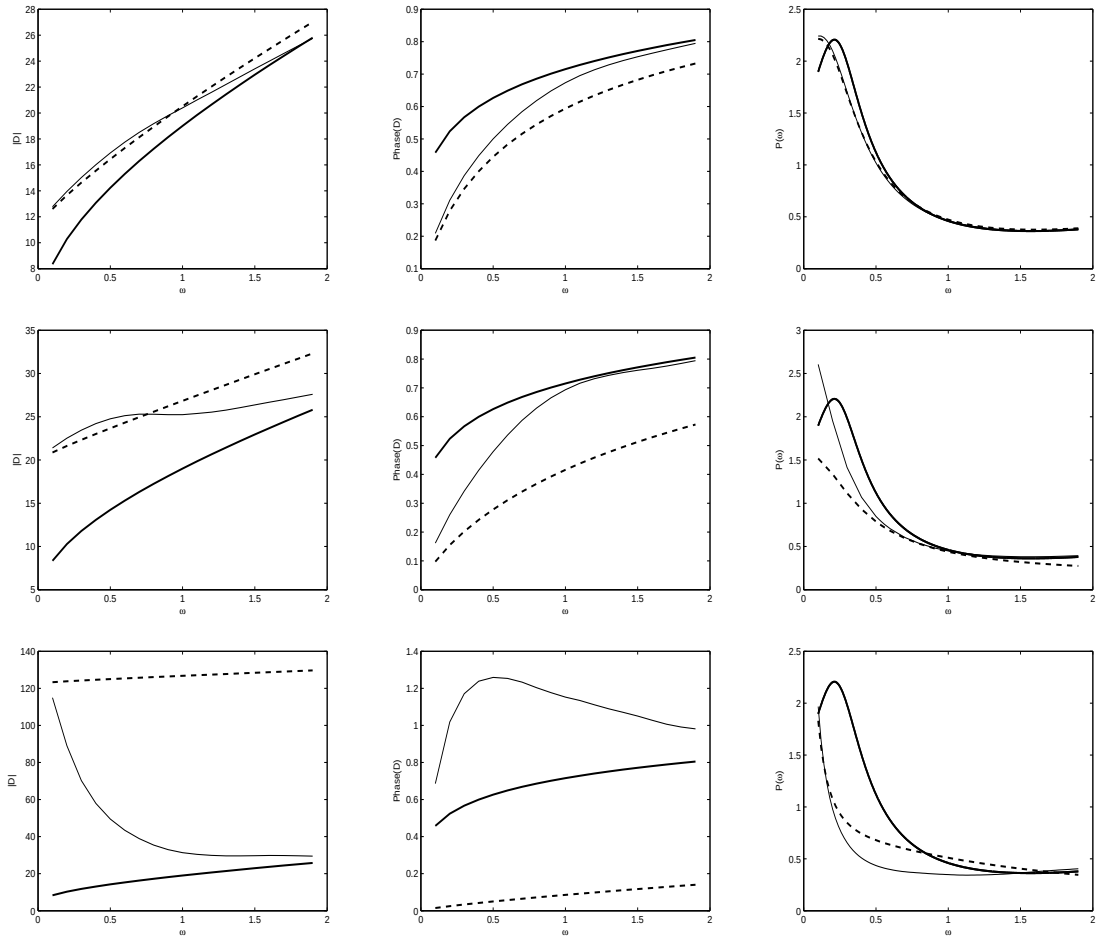

FIG. 5: Case B2: Modulus of Drag (Left Column) and Phase of Drag (Middle Column) exerted upon the microcantilever, as well as corresponding thermal spectra (Right Column), predicted when $\Lambda_0 = 10$, $\bar{R}_f = 1$, $\bar{R}_s = 0.51$ and (first row) $\Delta = 2$, (second row) $\Delta = 1$ and (third row) $\Delta = 0.2$.

its width so that $R^* = 10\mu m$. This, in turn, leads to greater levels of inertia in the flow, $\bar{R}_f = 100$ (and, to a lesser extent, in the sample, $\bar{R}_s = 5.1$). From the accompanying drag profiles, we see that the transition between the inelastic and sample-free limits in this regime takes place at lower frequencies than in Case A2, and below those at which the resonant peak in the thermal spectrum occurs. We see that this results in compliant effects disappearing from the thermal spectra, with the thermal spectrum closely following that produced in the absence of a sample, in spite of the effective stiffness being identical to that considered in Case A2 (i.e. $\Lambda_0 = 10$).

Even if flow inertia is kept at moderate levels (e.g. $\bar{R}_f = 10$), compliant effects can disappear

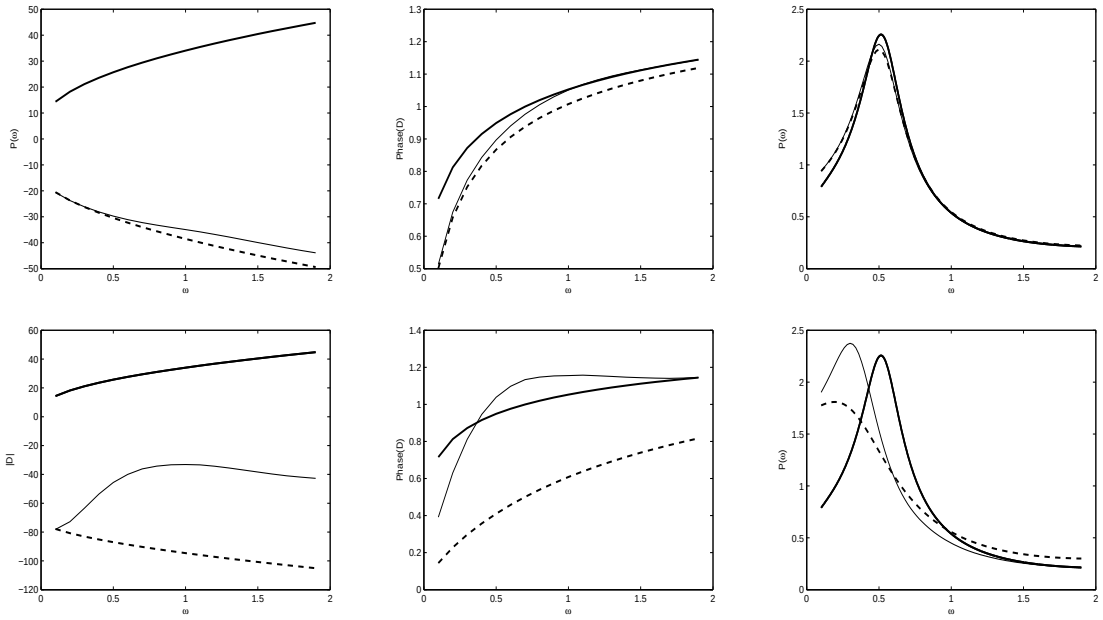

FIG. 6: Case B3: Modulus of Drag (Left Column) and Phase of Drag (Middle Column) exerted upon the microcantilever, as well as corresponding thermal spectra (Right Column), predicted when $\Lambda_0 = 10$, $\bar{R}_f = 10$, $\bar{R}_s = 1.61$ and (first row) $\Delta = 1$, (second row), $\Delta = 0.2$.

from the thermal spectra if the effective stiffness Λ_0 becomes too low. Let us consider Sample B, which has a Youngs Modulus of $E = 10^3 \text{km/ms}^2$, hence smaller than that of Sample A. For the parameter regime applied in Case A2, where compliant effects were previously evident in the thermal spectrum when $\Delta = 0.2$, we now observe a thermal spectrum which closely follows the sample-free limit (see Figure 4). The degree of flow inertia is the same as it was in Case A2 ($\bar{R}_f = 10$, although there is slightly more inertia in the sample), yet the effective stiffness is $\Lambda_0 = 1$, suggesting that the sample is so compliant that it offers very little hydrodynamic interaction with the microcantilever.

However, compliant effects can be established in the spectra of Sample B by decreasing the microcantilever's resonant frequency to $\omega_0^* = 10^5$ (see Case B2). This increases the effective stiffness to $\Lambda_0 = 10$, but at the same time decreases the characteristic flow inertia to $\bar{R}_f = 1$. This does result in distinct spectra for compliant samples, as shown in Figure 5 (which in this case remain distinct even at $\Delta = 1$). These spectra are somewhat over-damped, however, due to the relatively low inertia in the flow (i.e. high viscous dissipation within the generated flows). This can be adjusted for by increasing the width of the microcantilever ($R^* = 10\mu$m),

whilst keeping $\omega_0^* = 10^5$ (such that we maintain $\Lambda_0 = 10$). The resulting drag profiles and thermal spectra are shown in Figure 6 (Case B3). It can be seen that the compliant spectrum remains distinct when $\Delta = 0.2$, but now with a better quality factor than in Case B2.

V. CONCLUSIONS

We have considered the elastohydrodynamics generated when a microcantilever is thermally-driven close to a compliant sample. This study extends earlier work that considers either full oscillatory Stokes flow interactions between a microcantilever and an inelastic substrate [9, 12, 14], or squeeze film interactions with a deformable surface that is very close to the microcantilever and behaves like a thin elastic sheet [16]. By contrast, the deformable sample modelled here can undergo general small-strain elastic deformations, and is subject to full Stokes flow interactions with the microcantilever.

Our results demonstrate that the elastic properties of the sample alone do not control the appearance of compliant effects in a microcantilever's thermal response. Rather we find that the nondimensional effective stiffness, Λ_0, and characteristic flow inertia, $\bar{R}_f$, should fall within a particular ranges in order for compliant effects to be observable. If Λ_0 is too large, the spectrum resembles that produce by an inelastic sample; if too small, the spectrum is largely indistinguishable from that produce when no sample is present. For a sample with a given Youngs Modulus, Λ_0 can be increased by decreasing the microcantilever's resonant frequency (and vice versa). However, altering the microcantilever's resonant frequency also modifies the levels of inertia in the flow. We find that if the flow inertia is too large, the thermal spectra become indistinguishable from the case where no sample is present. This suggests that detection of sample compliance in the thermal spectra requires careful consideration of the operating conditions. For example, for the cases considered here, an increase in microcantilever width from 3μm to 10μm was seen to effectively remove sample compliance from the thermal spectra for Sample A.

These subtleties in the elastohydrodynamics illustrate the challenges associated with inferring micromechanical properties from microcantilever responses in general. The elastohydrodynamical analysis does simplify if one considers a squeeze film regime and a sample that can be modelled as an elastic half-space, as done by Gavara *et al.* [15], who examined the material properties of a layer of gel using a microprobe located at a distance of 100nm (using

mechanically-driven, rather than thermally-driven, microcantilever oscillations). However, for a non-layer-like sample, our results suggest significant elastic displacements occur outside of an asymptotically-small, near-contact region (see Appendix A 3). Hence it is therefore debatable whether a squeeze-film/elastic-half-space model would fully capture the elasto-hydrodynamics generated when the sample has a finite size. Moreover, the quality factor of the spectra tend to be impaired in these squeeze-film regimes, where viscous dissipation dominates the hydrodynamic loading upon the microcantilever. Nonetheless, through a full numerical treatment, we have shown that distinctive compliant effects can be generated in the thermal spectra for a sample with finite extent, by tailoring certain dimensional parameters appropriately (for the cases considered here $\Lambda_0 = \bar{R}_f = 10$ appear to yield distinctive compliant spectra; see also Appendix A 2). However, it remains to be seen whether the associated inverse problem can always be solved in practice, which would enable material properties to be inferred from the compliant thermal spectra.

In terms of potentially valuable extensions to the model, the manner in which the sample is adhered to a substrate could be an important factor. In addition, it could be valuable to extend the study to consider a wider range of sample rheologies. Also, it might be useful to consider the samples as (non-linearly) deformable capsules [20], which would allow for a viscoelastic response, and better represent some biological materials.

Acknowledgements

The authors wish to acknowledge the contribution of the NeSI high-performance computing facilities at the University of Auckland and the staff at NeSI and Centre for eResearch. New Zealand's national facilities are provided by the New Zealand eScience Infrastructure (NeSI) and funded jointly by NeSI's collaborator institutions and through the Ministry of Business, Innovation and Employment's Infrastructure programme. URL http://www.nesi.org.nz.

APPENDIX A: SINGULARITY SOLUTIONS

1. Fundamental Flow Solutions

The two-dimensional oscillatory Stokeslet is given by [18]

$$S_{ij}(\hat{\boldsymbol{x}};\lambda) = \frac{2}{\lambda^2}\left(\frac{\delta_{ij}}{r^2} - 2\frac{\hat{x}_i\hat{x}_j}{r^4}\right) - 2\left(\delta_{ij} - \frac{\hat{x}_i\hat{x}_j}{r^2}\right)K_0(\lambda r) - \frac{2}{\lambda}\left(\frac{\delta_{ij}}{r} - 2\frac{\hat{x}_i\hat{x}_j}{r^3}\right)K_1(\lambda r), \quad \text{(A1)}$$

recalling that $\hat{\boldsymbol{x}} = (\hat{x}_1, \hat{x}_2) = \boldsymbol{x} - \boldsymbol{x}_0$ ($r = |\hat{\boldsymbol{x}}|$, $\delta_{ij} = 1$ if $i = j$, and is zero otherwise). The accompanying stress tensor can be computed to be

$$\begin{aligned} T_{ijk}(\hat{\boldsymbol{x}};\lambda) = &\left(2\frac{\hat{x}_j\delta_{ik}}{r^2} - 8\frac{\delta_{ij}\hat{x}_k}{\lambda^2 r^4} - 8\frac{\delta_{ik}\hat{x}_j}{\lambda^2 r^4} - 8\frac{\delta_{jk}\hat{x}_i}{\lambda^2 r^4} + 32\frac{\hat{x}_i\hat{x}_j\hat{x}_k}{\lambda^2 r^6}\right) \\ &+ \left(4\frac{\delta_{ik}\hat{x}_j}{r^2} + 3\frac{\delta_{jk}\hat{x}_i}{r^2} + 3\frac{\delta_{ij}\hat{x}_k}{r^2} - 12\frac{\hat{x}_i\hat{x}_j\hat{x}_k}{r^4}\right)K_0(\lambda r) \\ &+ 2\lambda\left(\frac{\delta_{ij}\hat{x}_k}{r} + \frac{\delta_{kj}\hat{x}_i}{r} - 2\frac{\hat{x}_i\hat{x}_j\hat{x}_k}{r^3} + 3\frac{\delta_{ij}\hat{x}_k}{\lambda^2 r^3} + 3\frac{\delta_{jk}\hat{x}_i}{\lambda^2 r^3} + 4\frac{\delta_{ik}\hat{x}_j}{\lambda^2 r^3} - 12\frac{\hat{x}_i\hat{x}_j\hat{x}_k}{\lambda^2 r^5}\right)K_1(\lambda r) \\ &+ \left(\frac{\delta_{ij}\hat{x}_k}{r^2} + \frac{\delta_{kj}\hat{x}_i}{r^2} - 4\frac{\hat{x}_i\hat{x}_j\hat{x}_k}{r^4}\right)K_2(\lambda r), \end{aligned} \quad \text{(A2)}$$

where K_0, K_1 and K_2 are modified Bessel functions.

2. Elliptically-Shaped Sample

We also considered the case an elliptically-shaped sample, using the same operating parameters as in Cases A1-A3. The resulting thermal spectra are shown in Figure 7 below.

3. Sample Deformations

In Figure 8 we show the elastic displacements for Cases A1-A3, at the resonant frequencies in the thermal spectra.

---

[1] Sader, J. E. 1998 Frequency response of cantilever beams immersed in viscous fluids with applications to the atomic force microscope. *J. Appl. Phys.* **84**.

[2] Basak, S., Raman, A. and Garimella, S. V. 2006 Hydrodynamic loading of microcantilevers vibrating in viscous fluids *J. Appl. Phys.* **99** 114906.

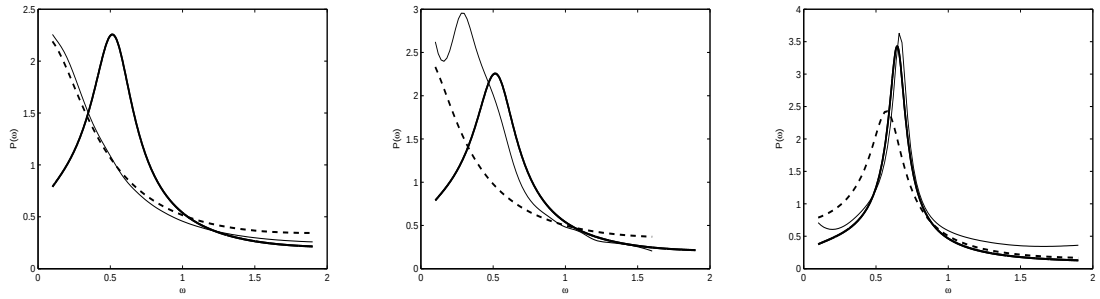

FIG. 7: Thermal spectra when the sample is elliptical in shape, with major (horizontal) axis 20μm and minor axis 10μm. Left-to-Right, spectra shown for samples E1-E3, which take the same parameters values as Cases A1-A3, respectively, i.e. (left) $\Lambda_0 = 100, \bar{R}_f = 10$, (middle) $\Lambda_0 = 10, \bar{R}_f = 10$, (right) $\Lambda_0 = 10, \bar{R}_f = 100$. In all three cases, $\Delta = 0.2$.

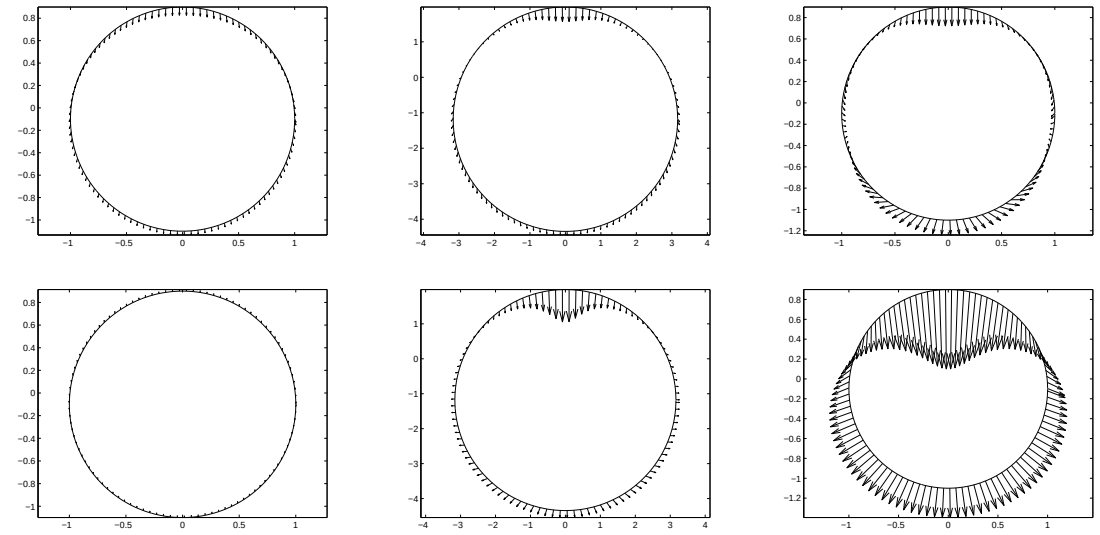

FIG. 8: Real (top) and imaginary (bottom) parts of elastic deformation, $\boldsymbol{u}$, when $\Delta = 0.2$ for Case A1 (left), Case A2 (middle) and Case A3 (right). These are calculated at (approximate) non-dimensional resonant frequencies $\omega = 0.2, 0.4, 0.6$, respectively.

[3] Chon, J.W.M., Mulvaney, P. and Sader, J. E. 2000 Experimental validation of theoretical models for the frequency response of atomic force microscope cantilever beams immersed in fluds. *J. Appl. Phys.* **87** 3978–3988.

[4] Paul, M. R. & Cross, M. C. 2004 Stochastic dynamics of nanoscale mechanical oscillators immersed in a viscous fluid. *Phys. Rev. Lett.* **92** (235501).

[5] Paul, M. R. & Cross, M. C. 2006 The stochastic dynamics of micron and nanoscale elastic cantilevers in fluid: fluctuations from dissipation *Nanotechnology* **17** 4502–4513

[6] Basak, S. and Raman, A. 2007 Hydrodynamic coupling between micromechanical beams oscillating in viscous fluids *Phys. Fluids* **19** 017105

[7] Paul, M. R. & Clark, M. T., and Cross, M.C. 2013 Coupled motions of microscale and nanoscale elastic objects in a viscous fluid *Phys. Rev. E* **88** (043012).

[8] Eysden, C.A. and Sader, J. E. 2007 Frequency response of cantilever beams immersed in viscous fluids with applications to the atomic force microscope: arbitrary mode order *J. Appl. Phys.* **101**.

[9] Green, C.P. and Sader, J.E. 2005 Small amplitude oscillations of a thin beam immersed in a viscous fluid near a solid surface *Phys. Fluids* **17** 073102.

[10] Green, C.P. and Sader, J.E. 2005 Frequency response of cantilever beams immersed in viscous fluids near a solid surface with applications to the atomic force microscope *J. Appl. Phys.* **98** 114913

[11] R. J. Clarke, S. M. Cox, P. M. Williams & O. E. Jensen 2005 The drag on a microcantilever oscillating near a wall. *J. Fluid Mech.* **545**.

[12] R. J. Clarke, O. E. Jensen, J. Billingham., A. Pearson & P. M. Williams 2006 Stochastic elastohydrodynamics of a microcantilever oscillating near a wall. *Phys. Rev. Lett.* **96** (050801).

[13] R. J. Clarke, O. E. Jensen & J. Billingham 2008 Three-dimensional elastohydrodynamics of a thin plate oscillating above a wall. *Phys. Rev. E* **78** (056310).

[14] Tung, R.C., Jana, A. and Raman, A. 2008 Hydrodynamic loading of microcantilevers oscillating near rigid walls *J. Appl. Phys.* **104** 114905

[15] N. Gavara R. S. Chadwick 2010 Noncontact microrheology at acoustic frequencies using frequency-modulated atomic force microscopy. *Nat. Methods* **7**.

[16] R.J.Clarke and S. Potnis 2011 Elastohydrodynamics induced by a rapidly moving microscopic body. *Proc. Roy. Soc. London A* **467**, 2852–2873.

[17] Pozrikidis, C. 1992 *Boundary Integral and Singularity Methods for Linearized Viscous Flow.* Cambridge University Press, 1992.

[18] Avudainayagam, A. & Geetha, J. 1993 Oscillatory line singularities of Stokes' flows. *Int. J. Engng Sci.* **31**, 1295–1299.

[19] Manolis, G.D. and Beskosi, D.E. (1981) Dynamics stress concentration studies by Boundary

Integrals and Laplace Transforms *Int. J. Num. Methods Engin.* **17**, 573–599

[20] Barthes-Biesel, D. (1980) Motion of a spherical microcapsule freely suspended in a linear shear flow *J. Fluid Mech.* **100**, 831–853